ACS APPLIED MATERIALS & INTERFACES

Research Article

Cite This: ACS Appl. Mater. Interfaces 2017, 9, 41246-41257

www.acsami.org

Anodes for Lithium-Ion Batteries Based on Type I Silicon Clathrate $Ba_8Al_{16}Si_{30}$ - Role of Processing on Surface Properties and Electrochemical Behavior

Ran Zhao,[†] Svilen Bobev,[‡] Lakshmi Krishna,[§] Ting Yang,[∥] J. Mark Weller,[∥] Hangkun Jing,[∥] and Candace K. Chan*[,∥]

[†]School of Molecular Sciences, Arizona State University, P.O. Box 871604, Tempe, Arizona 85287, United States

[‡]Department of Chemistry and Biochemistry, University of Delaware, Newark, Delaware 19716, United States

[§]Department of Physics, Colorado School of Mines, Golden, Colorado 80401, United States

[∥]Materials Science and Engineering, School for Engineering of Matter, Transport and Energy, Arizona State University, P.O. Box 876106, Tempe, Arizona 85827, United States

S *Supporting Information*

ABSTRACT: Type I silicon clathrates based on $Ba_8Al_ySi_{46-y}$ ($8 < y < 12$) have been studied as potential anodes for lithium-ion batteries and display electrochemical properties that are distinct from those found in conventional silicon anodes. Processing steps such as ball-milling (typically used to reduce the particle size) and acid/base treatment (used to remove nonclathrate impurities) may modify the clathrate surface structure or introduce defects, which could affect the observed electrochemical properties. In this work, we perform a systematic investigation of $Ba_8Al_ySi_{46-y}$ clathrates with $y \approx 16$, i.e, having a composition near $Ba_8Al_{16}Si_{30}$, which perfectly satisfies the Zintl condition. The roles of ball-milling and acid/base treatment were investigated using electrochemical, X-ray diffraction, electron microscopy, X-ray photoelectron and Raman spectroscopy analysis. The results showed that acid/base treatment removed impurities from the synthesis, but also led to formation of a surface oxide layer that inhibited lithiation. Ball-milling could remove the surface oxide and result in the formation of an amorphous surface layer, with the observed charge storage capacity correlated with the thickness of this amorphous layer. According to the XRD and electrochemical analysis, all lithiation/delithiation processes are proposed to occur in single phase reactions at the surface with no discernible changes to the crystal structure in the bulk. Electrochemical impedance spectroscopy results suggest that the mechanism of lithiation is through surface-dominated, Faradaic processes. This suggests that for off-stoichiometric clathrates, as we studied in our previous work, Li^+ insertion at defects or vacancies on the framework may be the origin of reversible Li cycling. However, for clathrates $Ba_8Al_ySi_{46-y}$ with $y \approx 16$, Li insertion in the structure is unfavorable and low capacities are observed unless amorphous surface layers are introduced by ball-milling.

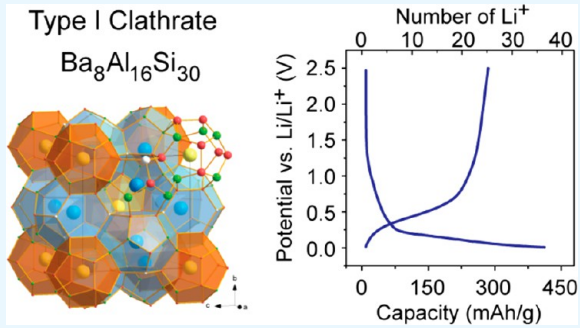

KEYWORDS: *Lithium-ion batteries, silicon, clathrate, anode, surface properties*

INTRODUCTION

Silicon clathrates[1] are known for their unique structures and potential as superconducting,[2−10] thermoelectric,[11−17] magnetic,[18,19] photovoltaic,[20,21] hydrogen storage,[22,23] and hard materials.[24] Compounds with the general formula M_xSi_{46} are known as type I clathrates (where M denotes the guest atoms, e.g. Ba, and $0 < x \leq 8$), with their structures made of large polyhedra fused together into an open-framework containing two pentagonal dodecahedra (Si_{20}) and six tetrakaidecahedra (Si_{24}) per unit cell. The guest atoms are found at the 6*d* (center of the Si_{24} cages) and 2*a* sites (center of the Si_{20} cages), while the clathrate framework is composed of Si at three crystallographic sites (6*c*, 16*i*, and 24*k*) as described with Wyckoff symmetry notation (Figure 1). Framework substitution, whereby some of the Si atoms are substituted with another element, is also common in clathrates. Example type I ternary clathrates that have been studied adopt the form $Ba_8X_ySi_{46-y}$ where *X* = Al, Ga, Zn, Cu, Ni, etc.[25−27] Such substituents help stabilize the clathrate structure by fulfilling the Zintl concept,[28] where each element achieves a closed shell state.[29] The net result is that the Fermi level is moved into a region with typically lower density of states, which can affect the electronic stability and transport properties.[27] For example, this condition is met in $Ba_8Al_{16}Si_{30}$, where the 16 valence electrons from the

Received: August 25, 2017
Accepted: October 5, 2017
Published: October 5, 2017

DOI: 10.1021/acsami.7b12810
ACS Appl. Mater. Interfaces 2017, 9, 41246−41257

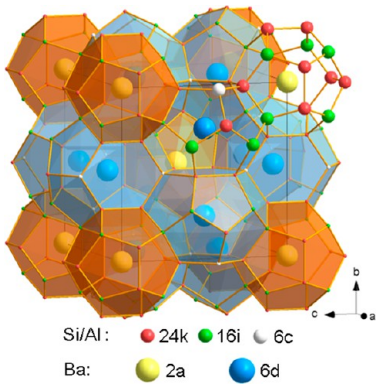

Figure 1. Combined ball-and-stick/polyhedral illustration of the type I clathrate $Ba_8Al_{16}Si_{30}$.

Ba guest atoms are balanced by substituting 16 Al atoms in place of Si atoms within the host framework. The electronic structures of clathrates can also be stabilized via the creation of framework vacancies, for example in $Ba_8Al_xSi_{42-(3/4)x}\square_{4-(1/4)x}$, $Ba_8Ge_{43}\square_3$ and $Cs_8Sn_{44}\square_2$, where $\square$ = vacancy).[13,14,23,30−32]

Recently, there has been much interest in the electrochemical properties of clathrates and their potential for applications in batteries.[33−39] Within the clathrate structure, Li could possibly occupy sites inside the Si_{20} and Si_{24} cavities (in the case of M deficiency), in addition to vacancy sites on the Si framework. Our previous first-principles density functional theory (DFT) studies showed that the clathrate structure could be stabilized when Li was inserted into Si framework vacancies or Ba guest atom vacancies within the Si_{20} cages; additionally, the calculations showed that multiple Li atoms can fit inside the Si_{24} cages.[35,37] In our group's previous experimental studies,[36] we found that ternary type I clathrates based on $Ba_8Al_ySi_{46-y}$ ($8 < y < 12$) displayed voltage-dependent redox characteristics distinct from those observed in diamond cubic Si, amorphous Si, and silicon oxides. Moreover, no discernible changes in the local bonding and crystalline structure of the type I clathrates were observed by nuclear magnetic resonance (NMR) or X-ray diffraction (XRD) after lithiation. The as-prepared clathrates investigated in our previous study had varied chemical compositions, reflecting the synthetic difficulties in the preparation of $Ba_8Al_ySi_{46-y}$ with defined y. The unambiguous compositional characterization of such clathrates is already nontrivial due to the low scattering contrast of Si and Al in both X-ray and neutron diffraction.[14,16] In our case, the as-synthesized samples also contained some unreacted precursors and side products such as Si and $BaSi_2$. In order to remove these nonclathrate species so that the electrochemical behavior of just the clathrate phase could be isolated, ball-milling followed by acid and base etching was employed. However, it is not known what role, if any, these processing steps played in the formation of additional defects in the clathrate structure, or the observed electrochemical properties of the clathrate composite electrodes.

To better understand these issues, here a systematic investigation of charge-compensated silicon clathrates with composition close to the stoichiometric Zintl condition (i.e., $Ba_8Al_{16}Si_{30}$) was performed. This would enable the evaluation of the electrochemical properties of silicon clathrates with a minimal number of defects such as framework vacancies. $Ba_8Al_{16}Si_{30}$ clathrate materials were prepared using arc melting or hot-pressing. Then, different processing steps (such as ball-milling, acid/base etching) were introduced and studied with XRD, X-ray photoelectron spectroscopy (XPS), Raman spectroscopy, electron microscopy, and electrochemical analysis to understand their role on the electrochemical behavior and other physicochemical features.

We find that very few Li atoms can be electrochemically inserted into the clathrates $Ba_8Al_ySi_{46-y}$ with $y \approx 16$, i.e., composition near $Ba_8Al_{16}Si_{30}$, which perfectly satisfy the Zintl concept.[28] Rather, the electrochemical processes resemble one dominated by surface adsorption behavior and low reversible lithiation capacities ~40 mAh/g. The acid/base etching treatment, while not affecting the crystallinity of the clathrate, caused the formation of an oxygen-terminated surface, which resulted in a decrease in the overall lithiation capacities. The introduction of ball-milling resulted in higher observed specific capacities, although not solely from the reduction of the particle size. High resolution transmission electron microscopy (TEM) observations showed that ball-milling led to the formation of amorphous surface layers on the clathrates. The presence of this amorphous layer was correlated to higher lithiation capacities, with the lithiation mechanism similar to a surface dominated, pseudocapacitive-like process rather than one relying on Warburg-type diffusion based on the electrochemical impedance spectroscopy analysis. These results show that for clathrates $Ba_8Al_ySi_{46-y}$ with $y \approx 16$, Li insertion in the structure is unfavorable unless amorphous surface layers are introduced. This suggests that for nonstoichiometric clathrates, as we studied in our previous work, Li^+ insertion at defects or vacancies on the framework may be the origin of reversible Li cycling.

EXPERIMENTAL SECTION

Synthesis of $Ba_8Al_{16}Si_{30}$ Clathrates by Arc-Melting. The clathrate samples prepared by arc-melting are named with the prefix "AM". In the arc-melting preparation, the elements Ba, Si, and Al (commercial grade materials with stated purity 99.9 wt %) were weighed in an Ar-filled glovebox (controlled O_2 and moisture atmosphere). The total weight of the starting materials was ca. 600 mg. The stoichiometric ratio was chosen to achieve a composition of $Ba_8Al_{16}Si_{30}$ within less than 0.1% error. Then, the materials were quickly transferred to the chamber of a custom-made arc-melter, which was evacuated to ca. 10^{-4} Torr and backfilled with high purity Ar. After the initial melting, the formed ingot was taken out and turned over. The melting process was repeated three times to ensure good homogeneity. The weight of the ingot at the end of the process was checked and the observed loss was less than 0.5%.

The as-made, arc-melted ingots were processed further, as shown in Figure 2. AM-1 refers to the sample obtained after the as-made, arc-melted ingot was ground by hand using a mortar and pestle. Then, this sample was ball-milled for 40 min (SPEX 8000, stainless steel grinding set) to yield AM-2. AM-2 was suspended in deionized water and treated with 3 M HCl for 12 h to remove the $BaSi_2$. After the acid treatment, the powder was recovered using vacuum filtration and washed with deionized water. Next, the powder was treated with 1 M NaOH for 12 h to remove amorphous or cubic Si, then recovered using vacuum filtration and washed with deionized water and dried to yield AM-3. AM-4 and AM-5 were obtained by ball-milling AM-3 after the etching treatment for 40 and 120 min, respectively.

Synthesis of $Ba_8Al_{16}Si_{30}$ Clathrates by Hot-Pressing. The clathrate samples prepared by hot-pressing are named with the prefix "HP". BaH_2 was used as the Ba source for the synthesis. Stoichiometric amounts of BaH_2, Al, and Si were mixed and loaded into an alumina boat, which was then heated in a tube furnace to 850 °C for 48 h under Ar atmosphere. Then, the powder was introduced into a $^1/_2$ in. graphite die and hot-pressed for 1 h at 850 °C and 100 MPa. Afterward, the sample was ground by hand using a mortar and pestle.

DOI: 10.1021/acsami.7b12810
ACS Appl. Mater. Interfaces 2017, 9, 41246−41257

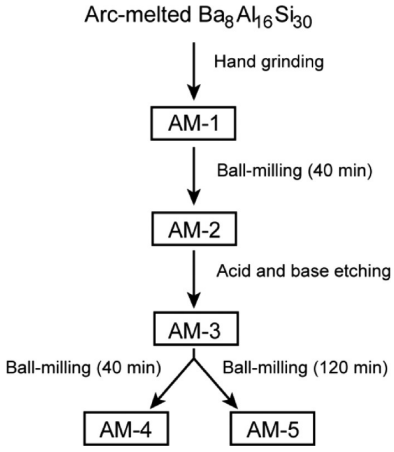

Figure 2. Schematic illustrating the processing performed on the $Ba_8Al_{16}Si_{30}$ clathrate samples prepared by arc-melting.

Materials Characterization. The silicon clathrates were characterized using wavelength dispersive X-ray spectroscopy (WDS), XRD, XPS, and Raman spectroscopy and imaged using scanning and transmission electron microscopy. The clathrate powders were prepared into composite electrodes with carbon black and binder and the electrochemical properties were evaluated in half cells with Li metal counter electrodes in nonaqueous electrolyte. More details about the materials characterization and electrochemical measurements are described in the Supporting Information (SI).

RESULTS AND DISCUSSION

Structural Characterization. The XRD pattern of AM-1 matched the reflections associated with $Ba_8Al_{16}Si_{30}$ (reference pattern: PDF 00-055-0373)[25] (Figure 3A). Additionally, some

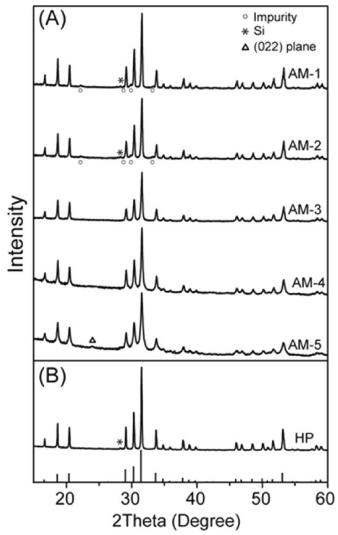

Figure 3. XRD patterns of $Ba_8Al_{16}Si_{30}$ samples prepared by (A) arc-melting, and (B) hot-pressing. The reference pattern for $Ba_8Al_{16}Si_{30}$ (PDF 00-055-0373) is shown on the bottom for comparison.

weak reflections that were not associated with the clathrate structure were observed at 2θ = 22.2, 28.4, 28.7, 29.9, and 33.3° (SI Figure S1A). The reflection at 28.4° is likely from the (111) reflections of diamond cubic Si, as this is commonly seen in clathrate syntheses as an indication of some unreacted precursor.[13,40,41] The other reflections are close to the positions of the (102), (211), (103), and (301) diffracting planes of $BaSi_2$, but the most intense reflection, for the (112) planes expected at 27.3°, was not observed in AM-1; hence it is unclear if $BaSi_2$ was present in the sample. These other reflections could be from a compound with $BaAl_4$-type structure, as suggested in previous studies.[13] $BaAl_2Si_2$ was also identified in previous studies on $Ba_8Al_ySi_{46-y}$ clathrate;[13,42] the peak at 2θ = 28.7 ° could be from the (211) plane of $BaAl_2Si_2$, but this assignment is also not unambiguous. Anno et al. have suggested the existence of $BaAl_2O_4$ as an impurity phase;[42] the reflection at 28.4° may have contributions from the (202) plane of that structure. However, given how the elemental Ba was stored and handled, the introduction of such a large amount of oxygen during the process is highly unlikely. We note that while the identity of the impurity phase(s) is not clear, the very weak intensity of the reflections is indicative of clathrate samples with phase purity of over 95% wt.

After ball-milling the AM-1 sample, the XRD peak positions remained the same, but the intensities were slightly altered (weakened and broadened) to a certain degree, which indicates a smaller particle size in AM-2 compared to AM-1. After acid and base treatment, the small impurity peaks disappeared from the XRD pattern of AM-3, confirming the removal of the impurity phases. The XRD pattern of AM-4, which was ball-milled for 40 min, had broader diffraction peaks due to the decrease in the particle size. After further ball-milling to make AM-5, the peaks were even broader and a small peak at 2θ = 24° was observed, which corresponds to the (022) plane of the Si clathrate. These results show that the acid/base etching and ball-milling do not affect the crystallinity within the bulk of the clathrate particles.

In the XRD pattern of the HP sample, only the crystalline peaks from the clathrate were observed, with only small amounts of cubic Si as impurity (Figure 3B), with the (111) reflections observed at 2θ = 28.4° (SI Figure S1B). The amount of cubic Si in the HP sample was estimated to be less than 1 wt % from the refinement of phase-fractions. The least-squares refinement results (SI Table S1) showed there was not a large difference in the lattice parameters of the clathrate samples, as they were all around 10.59 Å. Both experimental and computational studies have shown that as the Al content in $Ba_8Al_ySi_{46-y}$ clathrate increases, there is a linear increase in the lattice constant, a, due to the substitution of Si by Al in the framework, with $\Delta a/\Delta y \approx 0.02$ Å.[12,27,28,33,43] Since these changes were not observed in our samples, we assume that they are very close in composition. A previous report also showed that shifts in the (2 3 11) reflection in the XRD pattern of silicon clathrates were characteristic of differences in Al content,[44] but this was not observed in our samples, as shown in SI Figure S2A. The microprobe analysis results also did not show large differences in the composition between the samples (SI Table S2). Hence, we assume that the samples can be described with composition $Ba_8Al_ySi_{46-y}$, where $y \approx 16$.

SEM Characterization. Scanning electron microscopy (SEM) imaging was employed to determine the particle sizes of the clathrates. The SEM images of AM-1 showed particle sizes of about 1−40 μm (Figure 4A). Some of the particles were around 2 μm in size, but the majority of the sample consisted of particles larger than 20 μm. After ball-milling for 40 min to form AM-2, the particle size was reduced to less than 5 μm (Figure 4B). When the ball-milling was followed by the acid and base treatment to make AM-3, the morphology was more uniform, with the size controlled under 2 μm (Figure 4C). Further ball-milling for 40 min did not cause a large change in

DOI: 10.1021/acsami.7b12810
ACS Appl. Mater. Interfaces 2017, 9, 41246−41257

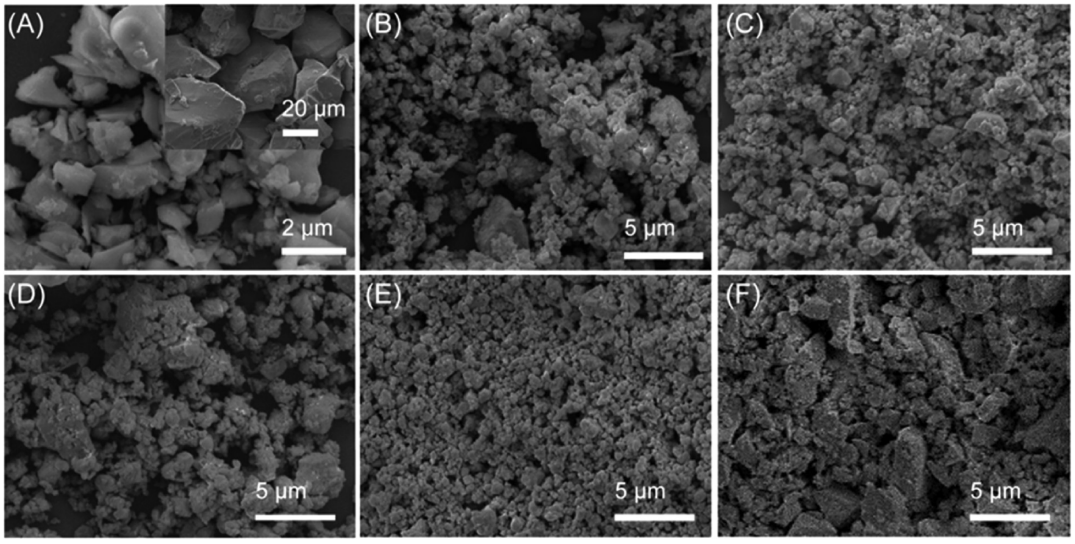

Figure 4. SEM images of different prepared $Ba_8Al_{16}Si_{30}$ samples (A) AM-1; (B) AM-2; (C) AM-3; (D) AM-4; (E) AM-5;(F) HP.

the particle sizes (AM-4, Figure 4D), but when the ball-milling time was increased to 120 min, the particle size decreased to about 1 μm (AM-5, Figure 4E). The SEM images showed that HP contained some particles with size of about 1−10 μm, but the majority of the particles were smaller than 5 μm (Figure 4F). Because of the fewer impurities and smaller particle sizes, no further processing was applied to the as-prepared HP sample.

XPS Characterization. XPS studies were performed to better understand the differences in the chemical surface states of the clathrate samples. As shown in Figure 5, the Ba $4d^{3/2}$ and Ba $4d^{5/2}$ peaks were observed at binding energies of 93.0 and 90.3 eV, respectively, whereas the Si $2p$ peak corresponding to the Si in the clathrate framework was found at 98.6 eV. Due to the interaction of the Si with Ba and Al, the binding energy of Si in the clathrate shifted to a lower energy level compared to that observed in diamond cubic Si.[45] The signal attributed to surface Si bound to oxygen was centered at approximately 102.5 eV, suggesting the presence of a native oxide in the as-prepared AM-1 and HP samples. This is consistent with previous studies identifying a native oxide on silicon clathrate surfaces.[36,46] Comparing the spectra for AM-1 and AM-2, the percentage of the total Si signal associated with the Si−O environment (76%) remained the same (SI Table S3), indicating that ball-milling did not affect this oxide layer. After the acid/base treatment, however, the Si−O peak intensity became stronger, and made up 94% of the Si spectrum, suggesting that the acid/base treatment oxidized the AM-3 clathrate surface. Additional ball-milling after the acid/base treatment resulted in an increase in the Si−Si peak intensity in AM-4 and AM-5 to 17% and 19% of the total signal (SI Table S3), respectively, which could be due to the exposure of fresh surfaces as the particles were ball-milled.

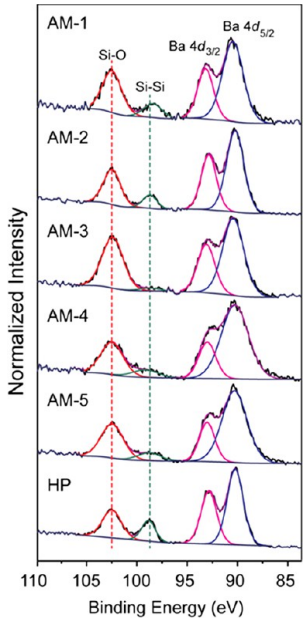

Figure 5. High resolution XPS spectra of AM-1, AM-2, AM-3, AM-4, AM-5, and HP clathrate samples. The green dashed line is at 98.6 eV and the red dashed line is at 102.5 eV.

Raman Spectroscopy Characterization. To further characterize the vibrational modes of the clathrates, Raman spectroscopy was performed. Previous studies demonstrated that the Raman spectrum of silicon clathrates is characterized by (1) low-frequency vibration bands associated with the rattling guest atoms, (2) a low frequency framework band, and (3) a high frequency framework band that describes how strongly the guest atoms are interacting with the framework. The high frequency framework band is observed at between 430 and 461 cm^{-1} in nonframework substituted clathrates,[8,47,48] for example, at 438 cm^{-1} in Ba_8Si_{46}.[8] When Al-substitution is used, the band redshifts due to the reduced mass when replacing Al with Si. For example, this framework band was observed at 517 and 508 cm^{-1} in $Ba_{7.5}Al_{13}Si_{29}$ and $Eu_{0.27}Ba_{7.22}Al_{13}Si_{29}$, respectively.[49] The redshift was also observed in the lowest frequency framework band, which is between 100 cm^{-1} to 200 cm^{-1} in the nonframework substituted clathrate,[8,48,50] and between 200 cm^{-1} to 400 cm^{-1} for the Al substitution silicon clathrate.[49]

The highest-frequency framework mode in our AM-1 and AM-2 samples was observed at 495 cm^{-1} (Figure 6). This mode red-shifted to 510.5 cm^{-1} in AM-3 after etching, but shifted back after further ball-milling, for example, for AM-5. The same trend was also found in the lowest-frequency framework

DOI: 10.1021/acsami.7b12810
ACS Appl. Mater. Interfaces 2017, 9, 41246−41257

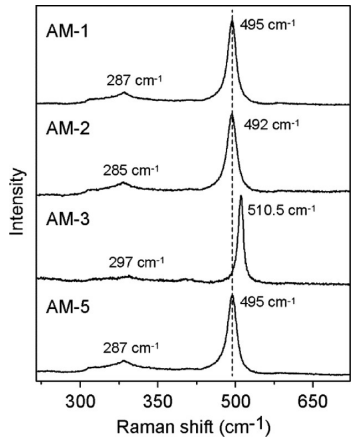

Figure 6. Raman spectra of AM-1, AM-2, AM-3, and AM-5. The dashed line represents a Raman shift of 495 cm^{-1}.

vibrations around 300 cm^{-1}. From the XPS analysis, the amount of Si−O bonding increased after etching, so the redshift observed in AM-3 is likely due to the formation of the surface oxide layer.

TEM Characterization. To better understand the surface structure of the different clathrate samples, transmission electron microscopy (TEM) characterization was performed (Figure 7). Selected-area electron diffraction (SAED) was also performed to assess the crystallinity of the particles. The samples were stable under the electron beam and no visible changes to the microstructure of the samples were observed during imaging. A thin amorphous layer less than 5 nm thick was observed in AM-1 (Figure 7A), and the SAED pattern showed distinct spots, indicating that the particles were predominately crystalline. After ball-milling, the amorphous surface layer became thicker in AM-2, in some cases more than 10 nm in thickness (Figure 7B). This shows that ball-milling can cause the surface of the clathrate particles to become amorphous. The TEM analysis of the sample after ball-milling and acid/base treatment, AM-3, displayed a nonuniform amorphous layer, which was in some cases only ∼5 nm thick (Figure 7C). This suggests that the acid/base treatment could have partially etched away the amorphous layer. The XPS analysis also indicated that acid/base treatment oxidized the surface, so the surface layer is likely a mixture of the amorphous material generated by ball-milling and the Si−O species produced by the acid/base treatment. The TEM images of AM-4 and AM-5 showed that further ball-milling introduced more amorphous regions. The AM-4 sample, which was ball-milled for 40 min, displayed an amorphous layer about 10 nm thick (Figure 7D), while the sample ball-milled for 120 min, AM-5, showed an even thicker layer of 10−20 nm thick (Figure 7E). However, the crystalline lattice fringes and electron diffraction ring pattern (Figure 7F) showed that the particle interiors were still crystalline, consistent with the XRD results (Figure 3).

Electrochemical Properties. The voltage curves obtained from galvanostatic cycling of the different samples are shown in Figure 8, while the capacity retention is shown in SI Figure S3. AM-1 exhibited a first charge (lithiation) capacity of 85 mAh/g and a first discharge (delithiation) capacity of 46 mAh/g, which decreased in subsequent cycles (Figure 8A). The $Ba_8Al_{16}Si_{30}$

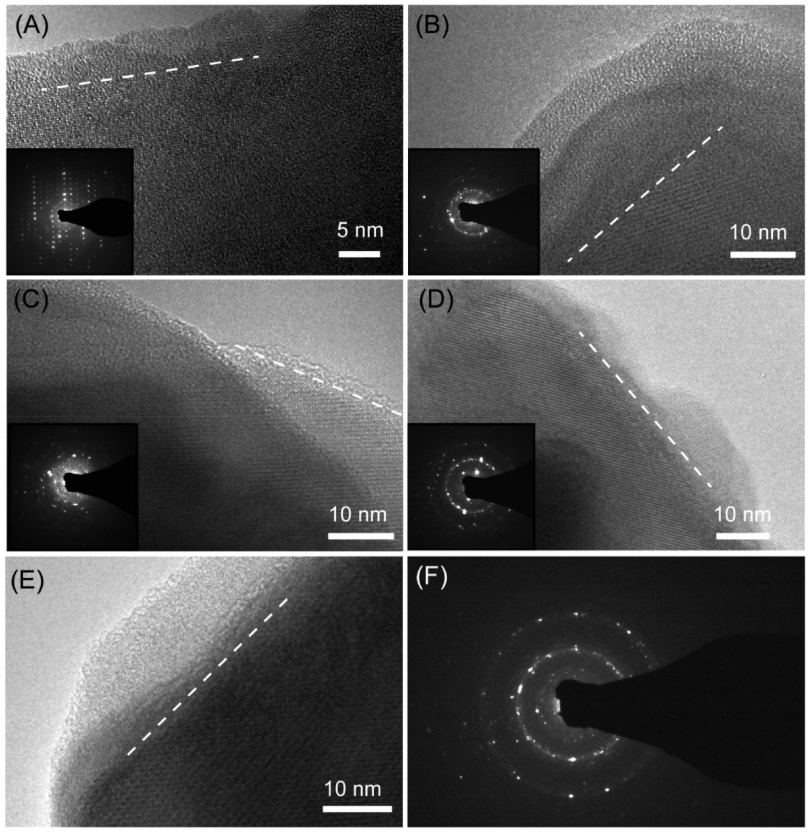

Figure 7. High-magnification TEM images and selected-area electron diffraction patterns for (A) AM-1, (B) AM-2, (C) AM-3, (D) AM-4, (E)(F) AM-5. The dashed line indicates the amorphous−crystalline interface.

DOI: 10.1021/acsami.7b12810
ACS Appl. Mater. Interfaces 2017, 9, 41246−41257

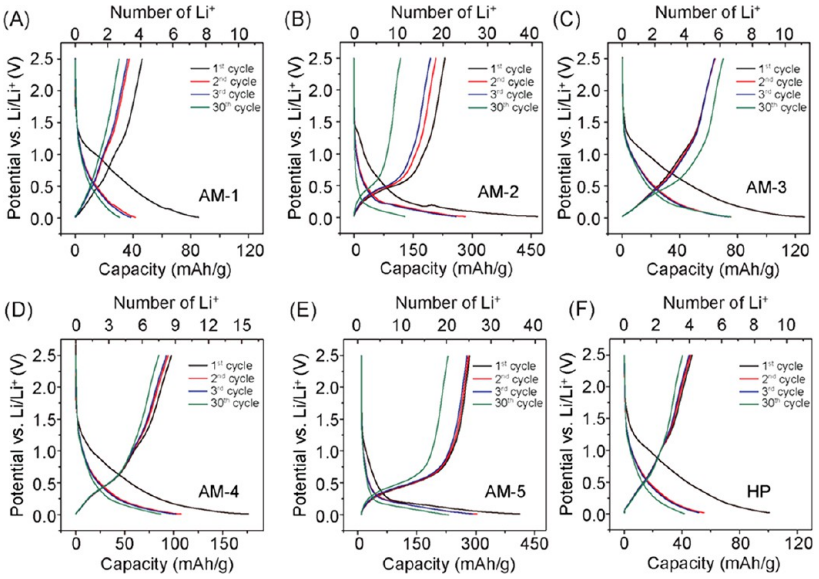

Figure 8. Voltage profile of first three cycles and thirtieth cycle for (A) AM-1, (B) AM-2, (C) AM-3, (D) AM-4, (E) AM-5, and (F) HP electrodes. The galvanostatic measurements were performed from 0.01−2.5 V vs Li/Li^+ range using a current density of 25 mA/g.

clathrate is expected to be a decent electronic conductor (semiconductor if fully charge compensated,[51] metallic-like if not precisely at the Zintl composition[13,14,30]), but the carbon black additive may not have been sufficient to ensure good electronic conductivity through the AM-1 composite electrode due to the large particle sizes.

As shown in Figure 8B, ball-milling AM-1 resulted in a large increase in capacity, with 472 and 276 mAh/g observed in the first charge and discharge cycle of AM-2. These capacities correspond to ca. 20 Li^+ reversibly inserted per clathrate formula unit in AM-2, compared to around 3 Li^+ for AM-1. Also notable, was that whereas the shape of the charge/discharge curves was rather linear in AM-1, in AM-2 a plateau feature was observed <0.2 V vs Li/Li^+. This increase in capacity after the sample was ball-milled can be explained by the decrease in particle size, as seen in the SEM imaging (Figure 4B), but may also be due to additional capacity from the electrochemical reaction of Li with the amorphous layers on the particle surfaces.

To better understand this, the capacities of the other samples were also studied. After the acid/base treatments were applied, AM-3 showed a 126 mAh/g charge and 64 mAh/g discharge capacity in the first cycle (Figure 8C), which is only 23−26% of the capacities of AM-2. Since the TEM imaging indicated that the amorphous layer was thinner after the acid/base treatment, the lower capacities in AM-3 compared to AM-2 could be due to removal of this layer of active material. Also, the layer rich in Si−O on the surface of the clathrate may have also played an inhibitory role on the reaction of Li with the clathrate. The AM-4 and AM-5 results further support these hypotheses, as ball-milling of AM-3 resulted in higher capacities, and both AM-4 and AM-5 had thicker amorphous layers and less surface oxide. As shown in Figure 8D,E, the first charge/discharge capacities were increased to 176 mAh/g and 98 mAh/g for AM-4 (40 min ball-milling) and 403 mAh/g and 276 mAh/g for AM-5 (120 min ball-milling), corresponding to increases in lithiation capacity by 40% and 220%, respectively, relative to AM-3. AM-5 displayed the largest number of Li reversibly inserted from all the samples studied, about 25 Li^+ per formula unit. From the SEM images (Figure 4D,E), the longer ball-milling times can help to improve the uniformity of the particle morphology and decrease the particle size, but not dramatically. The XPS (Figure 5) and Raman spectroscopy (Figure 6) results support the exposure of nonoxide covered surfaces in AM-4 and AM-5, while the TEM analysis showed more amorphous layers were generated with the extended ball-milling time. From these observations, it appears that these two features are the main contributors to the higher specific capacities in these two samples.

To further verify this, the performance of HP was evaluated. Despite the particle sizes of HP being similar to those for AM-2 based on the SEM results, the first charge/discharge capacities for HP were only 107 mAh/g and 53 mAh/g (Figure 8F), much lower than what was observed in AM-2. Therefore, HP is more similar in performance to AM-1, which was also not ball-milled. This suggests that the smaller particle sizes are not the main reason for the large capacity gain in the ball-milled samples, but that the amorphous phases introduced by the ball-milling process may play a major role in the electrochemical reaction of the clathrate materials with Li^+.

The long-term galvanostatic cycling results (SI Figure S3) showed that the capacities of all of the samples decreased after the first few cycles. The capacity of AM-1 stabilized at 37 mAh/g after 20 cycles, while due to the smaller particle size, HP had a higher capacity of 41 mAh/g (SI Figure S3A). AM-3 and AM-4 displayed capacities of 78 mAh/g and 95 mAh/g after 100 cycles, respectively (SI Figure S3B). The capacities for AM-3 and AM-4 also slightly increased in the later cycles, which implies some sort of activation process. This could be related to the removal of the silicon oxide surface during the electrochemical reaction, which would lead to more exposure of clathrate surface. The similar cycling behavior of AM-3 and AM-4 suggests that the 40 min of ball-milling was not sufficient to expose all of the clathrate surface. The ball-milled samples AM-2 and AM-5 showed the most capacity fade; a capacity of 79 mAh/g was observed from AM-2 after 100 cycles, and 136 mAh/g from AM-5 after 100 cycles (SI Figure S3C). However, the capacity retention in these materials was better than those we observed in the nonstoichiometric clathrates in our previous work[36] at the same current density. XRD analysis of the

DOI: 10.1021/acsami.7b12810
ACS Appl. Mater. Interfaces 2017, 9, 41246−41257

electrodes after the first lithiation and after 100 cycles did not show a decrease in peak intensity (SI Figure S2B), suggesting that amorphization of the clathrate structure is not occurring as a result of the electrochemical lithium insertion reaction.

To better understand the mechanism of lithiation into the clathrate samples, the differential charge (dQ) plots (Figure 9)

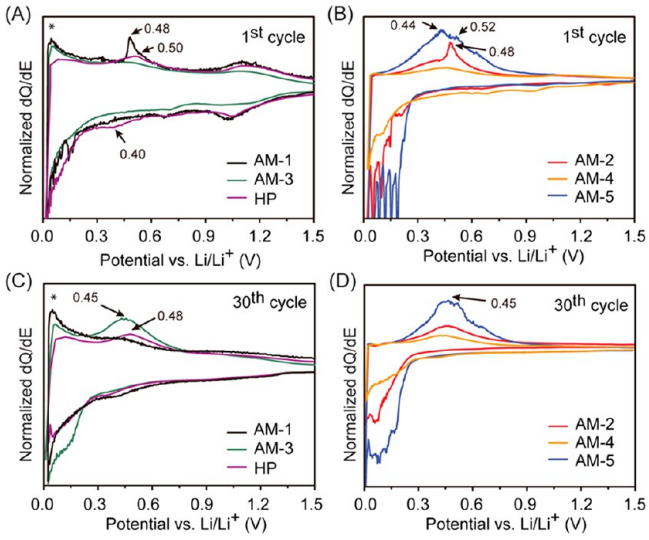

Figure 9. Differential charge (dQ) plots of AM-1, AM-3, AM-4, and HP-1 for the (A) first cycle; (C) thirtieth cycle. dQ plots of AM-2 and AM-5 for the (B) first cycle; (D) thirtieth cycle. * indicates the Li reaction with carbon black.

were analyzed to obtain additional information regarding the potential-dependent electrochemical reactions. The peak centered at around 1 V in the dQ plots of AM-1 and HP (Figure 9A) is likely due to reduction of the electrolyte to form a solid electrolyte interphase (SEI) layer.[52] These features cannot be discerned in the following cycles, which is consistent with the SEI formation predominately occurring during the first cycle. This SEI formation peak was not as obvious in the ball-milled samples (Figure 9B), which is consistent with the amorphous surface layer in those samples creating a different interface with the electrolyte, which might result in different SEI formation properties. At lower potentials where the reaction between the clathrate and Li is expected to occur, different characteristics were observed in the different samples. The linear voltage profiles (Figure 8) for AM-1, AM-3, and HP along with the capacitor-like dQ plots (Figure 9A) suggest a surface-dominated, capacitive adsorption mechanism[53] in these samples. However, peaks more characteristic of Faradaic reactions were dominant in the dQ plots of AM-2, AM-4, and AM-5 (Figure 9B).

To better interpret the features in the dQ plots, an AM-3 electrode containing 10 wt % polyvinylidene difluoride (PVDF) as binder but no carbon black additive was prepared to identify the clathrate characteristics without interference from Li ion adsorption on the carbon black. As shown in SI Figure S4A, a broad reduction peak was observed at 0.4 V and a broad peak was observed centered at 0.46−0.5 V during oxidation. To identify the potential-dependent redox characteristics of the carbon black, an Al_2O_3 electrode with carbon black and PVDF (80:10:10 by wt %) was prepared and cycled over the same potential range. The dQ plot of the Al_2O_3 electrode showed capacitive double-layer charging behavior, with the only pronounced peak found at 0.035 V during oxidation (SI Figure S4B). As Al_2O_3 is considered to be electrochemically inactive to lithium,[54] the observed electrochemical reaction in this electrode is attributed to the reaction of Li with carbon black. Therefore, we assign the peaks found at around 0.4−0.5 V in Figure 9A,C to the clathrate, while the feature at 0.035 V in the oxidation originates from the carbon black. This carbon black feature is less noticeable in the dQ plots for AM-2, AM-3, and AM-5 (Figure 9B,D) due to the higher capacity contribution of the reaction of Li with the clathrates. The potentials of these broad peaks were similar to those observed in our previous work on off-stoichiometric clathrates (nominal composition $Ba_8Al_8Si_{30}$)[36] with reduction starting below ~0.3 V vs Li/Li^+, and suggest a single-phase, solid solution lithiation mechanism. For both groups of samples, these characteristics were maintained even after 30 cycles (Figure 9C,D).

Similar to our previous observations,[36] the voltage-dependent redox characteristics in these clathrate samples were distinct from those observed in diamond cubic Si, amorphous Si, and SiO. The dQ plot associated with cubic Si reacting with Li is characterized by a sharp peak at 0.125 V vs Li/Li^+ associated with a two-phase reaction to form amorphous lithium silicide, and a peak near 50 mV which is attributed to the formation of $Li_{15}Si_4$.[55,56] Lithiation of amorphous Si occurs as two single-phase reactions, which manifest as broad peaks centered at 0.25 and 0.1 V vs Li/Li^+ in the dQ plots.[57] SiO undergoes a conversion reaction with Li to form lithium silicates and Li_2O, which results in a sharp peak at 0.25 V and a broad one at around 0.1 V vs Li/Li^+ in the dQ plot.[58]

During the delithiation process, broad peaks centered at 0.45 V vs Li/Li^+ were observed in all of the samples. Compared with the off-stoichiometric clathrates, which exhibited a broad discharge peak at 0.4 V vs Li/Li^+ in the dQ plots,[36] the discharge voltage of clathrates studied here are higher, which is likely due to the difference of the composition (i.e., Al/Si ratio). Again, the dQ plots during discharge do not match those observed in electrodes made of cubic Si, amorphous Si, or SiO. The cubic Si undergoes a two-phase delithiation reaction at about 0.43 V,[56] while Li is removed in two single-phase reactions centered at 0.3 and 0.5 V vs Li/Li^+ in amorphous Si.[57] Delithiation of charged SiO shows similar characteristics as those found in amorphous Si. The sharp peaks at 0.48 V observed in AM-1 and AM-2 are attributed to impurities, since these samples had not been treated with the acid and base. Because these samples contained residual cubic Si, these redox peaks may originate from the two-phase delithiation of c-$Li_{15}Si_4$ formed by from the reaction of Li with this residual Si during charging.[56]

To better understand the mechanism of lithiation and delithiation into the clathrate particles, electrochemical impedance spectroscopy (EIS) measurements were performed for pristine AM-2, AM-3, and AM-5 electrodes and at different states of charge (SOC) during lithiation and depths of discharge (DOD) during delithiation (SI). The potential vs time profiles for the measurements are shown in SI Figure S5, while the Nyquist plots are shown in Figure 10 for small impedance values and in SI Figure S6 for larger values. At the highest frequency (100 kHz), the impedance (<30 Ω) is dominated by the series resistance arising from the external cell connections and ionic conductivity of the electrolyte,[59] which can be determined in the Nyquist plot by the intercept of the curve with the real axis. For all three samples, the impedance response of the pristine electrodes was characterized by a

DOI: 10.1021/acsami.7b12810
ACS Appl. Mater. Interfaces 2017, 9, 41246−41257

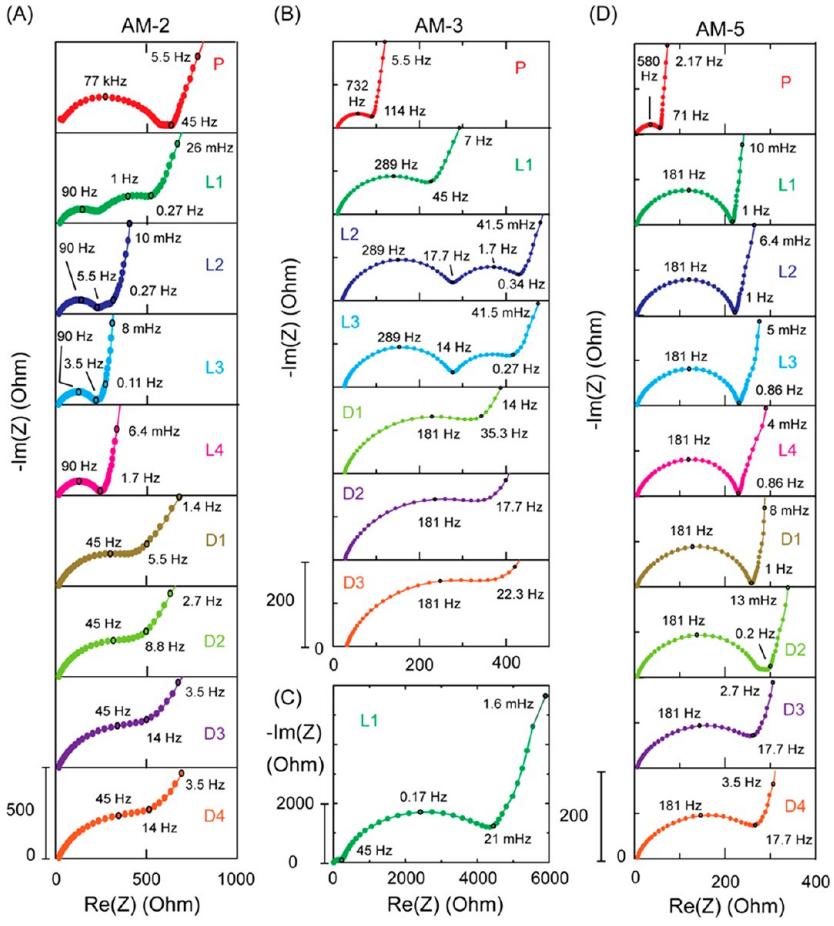

Figure 10. Nyquist plots for (A) AM-2, (B) AM-3, and (D) AM-5 obtained at different SOC and DOD with select frequencies labeled. (C) is showing AM-3-L1 at higher impedances. The capacities for each SOC and DOD are shown in SI Figure S5. (*P* = pristine; L1 = first lithiation step, L2 = second lithiation step, etc.; D1 = first delithiation step, etc.).

depressed semicircle at high frequencies and nearly vertical tail at low frequencies, indicating a capacitor-like response and blocking character of the electrode prior to lithiation. These features have also been observed in fresh graphite anodes prior to formation of the SEI layer, with the high frequency semicircle attributed to the porosity of the electrode, and the low frequency behavior due to the adsorption of ions at the electrode/electrolyte interface.[60,61]

Upon charging AM-2, two depressed arcs were observed, one with maximum impedance at 90 Hz and the other at 1 Hz (AM-2-L1 in Figure 10A). The higher frequency arc centered at 90 Hz did not change as the potential decreased in the subsequent charging steps and is hence attributed to a contact impedance,[62−64] for instance between the electrode particles with each other or the current collector. The medium frequency arc with maximum impedance at 1 Hz is attributed to the charge transfer impedance associated with the Li reaction with the clathrate since the diameter of this arc decreased as lithiation proceeded. With further lithiation, the impedance of the low frequency tail also decreased. However, the phase angle at low frequencies remained lower than −45°, indicating that the low frequency process is not one described by Warburg-type, solid-state Li^+ diffusion. This is more readily observed in the Bode plot (Figure 11A), where the phase angle at low frequencies is close to −90°, similar to the features found in double layer capacitors and pseudocapacitors[65−67] where surface-based adsorption and Faradaic processes predominate. The peak in the Bode plot observed at around 100−1000 Hz is attributed to the aforementioned contact impedance, while the small peak observed at around 10 Hz in AM-2 after the first lithiation step (AM-2-L1) is attributed to the charge transfer impedance. The Nyquist plots obtained after lithiation could be fitted (SI Table S4) to an equivalent circuit that uses a resistor to represent the series resistance, a resistor and constant phase element (CPE) in parallel to represent the impedance of the first semicircle, a resistor and CPE to represent the impedance of the second semicircle, and another CPE to take into account the blocking character of the low frequency tail (SI Figure S7A).

The EIS results for sample AM-3 during lithiation showed similar features as for AM-2, but the charge transfer resistance was much higher, consistent with the presence of the oxide-rich surface layer. This is seen by the larger semicircle in the Nyquist plot for AM-3 after the first lithiation step (AM-3-L1 in Figure 10C) and peak around 10 Hz in the Bode plot (Figure 11C). Similar to sample AM-2, the charge transfer impedance decreased as more lithium was inserted, which is attributed to the reduction of the surface oxide layer during charging (SI Table S4). On the other hand, in contrast to AM-2 and AM-3, the EIS results for AM-5 did not show much variation as a function of lithium content. The Nyquist plots for AM-5 (Figure 10D) showed a depressed semicircle with maximum impedance observed at 181 Hz and long tail below ∼1 Hz, and there was no emergence of a distinct medium frequency arc as

DOI: 10.1021/acsami.7b12810
ACS Appl. Mater. Interfaces 2017, 9, 41246−41257

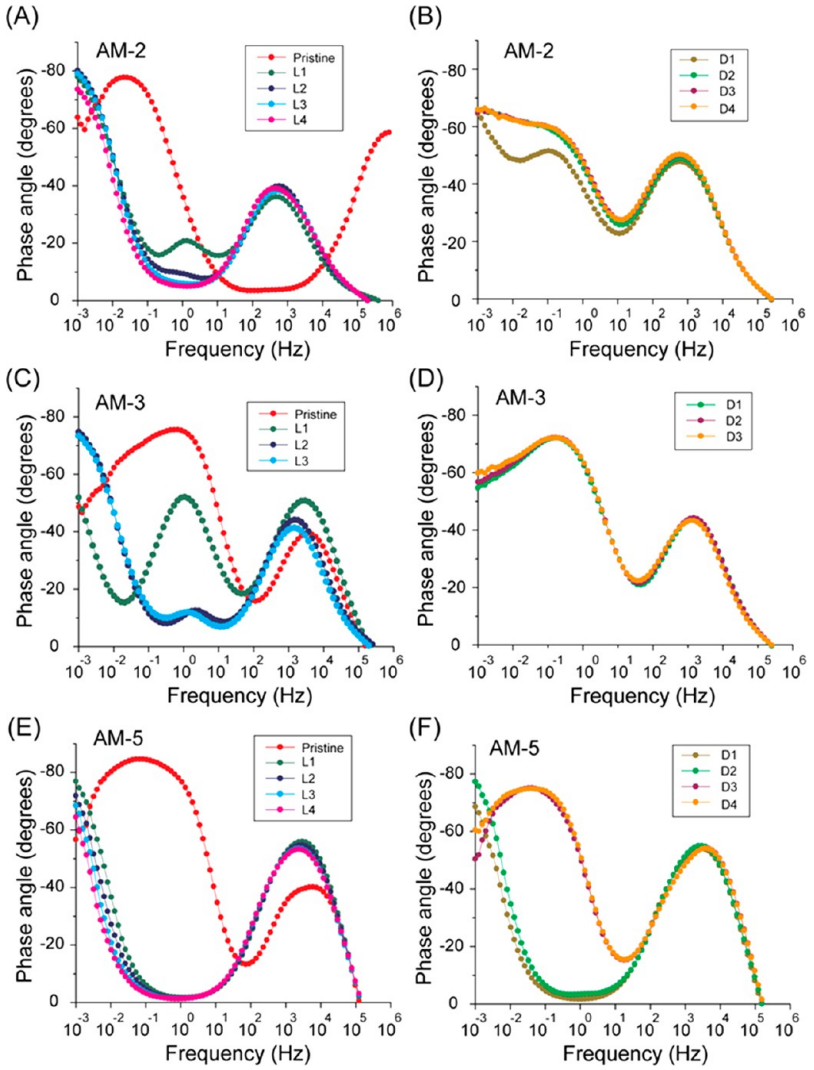

Figure 11. Bode plots showing the phase angle vs frequency for (A)(B) AM-2, (C)(D) AM-3, and (E)(F) AM-5 during lithiation and delithiation. The capacities for each SOC and DOD are shown in SI Figure S5. (*P* = pristine; L1 = first lithiation step, L2 = second lithiation step, etc.; D1 = first delithiation step, etc.).

lithiation proceeded. The Bode plot (Figure 11E) also showed that the phase angle at low frequencies remained less than −60° during lithiation. These results imply a pseudocapacitive-like, surface dominated Faradaic process for AM-5, which is consistent with the features in the dQ plots. This is notably different from conventional silicon anodes, which display clear Warburg diffusion behavior indicative of solid-state Li^+ diffusion through the bulk, as seen by a tail at 45° from the real impedance axis in the Nyquist plots or phase angle close to −45° at low frequencies in the Bode plots.[59,68,69]

Upon delithiation, the high and medium frequency arcs in the Nyquist plots for all three samples merged into one depressed semicircle and the impedance of the low frequency tail greatly increased. The change in low frequency impedance during lithiation and delithiation is more readily seen in the plots in SI Figure S6. The increase in impedance during delithiation has also been observed in conventional anodes[59,62] and can arise from a number of sources, such as a change in phase or morphology that affects the diffusion through the electrode or SEI layer. The Bode plot of the discharged electrodes shows that the phase angles at low frequencies shift closer to −45°, suggesting that the process becomes Warburg-like during delithiation. However, it is possible that this feature arises from the solid-state diffusion of Li through the SEI layer. The EIS data for AM-2 and AM-3 during delithiation, and AM-5 during both lithiation and delithiation, could be fit to the equivalent circuit shown in SI Figure S7B, with one fewer resistor and constant phase element in parallel compared to the circuit used to model the electrodes during lithiation. The contact impedance is not observed as a distinct arc in the AM-5 electrodes during lithiation likely due to the smaller particle sizes, which may improve the electronic contacts between the particles.

Overall, these studies point to an interesting conclusion, namely that while the silicon clathrate structure close to the Zintl condition can be lithiated, the surface properties play a crucial role in the observed capacities. We find here that the extended ball-milling enables about 25 Li^+ per formula unit (for AM-5) that can be reversibly cycled. However, this is much lower than the 40−50 Li^+ per formula unit we observed in the off-stoichiometric clathrates (nominal composition $Ba_8Al_8Si_{38}$) studied in our previous work,[36] which were not subjected to this extended ball-milling. This suggests that Li insertion at defects or framework vacancies that may be present in off-

DOI: 10.1021/acsami.7b12810
ACS Appl. Mater. Interfaces 2017, 9, 41246−41257

stoichiometric clathrates may lead to increased capacities. There has been experimental evidence showing that Li can occupy framework vacancies in the germanium clathrates $K_8Li_\delta Ge_{46-\delta}$ ($0 \leq \delta \leq 2.3$)[70] and $Na_{16}Cs_8Li_xGe_{136-x}$ ($x \approx 2.8$),[71] but the confirmation of a similar phenomenon in silicon clathrates is still needed. In the absence of defects, the lithiation capacity of the clathrates close to the Zintl condition is low, but can be increased by more than 5 times when an amorphous layer is generated by ball-milling. After acid and base treatment, the capacity was decreased likely due to the removal of some of the amorphous layer and introduction of a surface oxide which greatly increased the charge transfer resistance. Ball-milling of the particles again after the acid and base treatment can decrease the particle size, remove the surface oxide, and generate a thicker amorphous layer, all of which result in an increase in the capacity. Regardless of the surface properties, the lithiation mechanism appears to be dominated by pseudocapacitive-like surface process, which is supported by the EIS and dQ analysis.

CONCLUSIONS

In conclusion, we performed a systematic investigation of the effect of processing steps on the structural and electrochemical properties of silicon clathrates. The results show that for the silicon clathrate at the Zintl condition, Li insertion into the structure is unfavorable unless amorphous surface layers are introduced using ball-milling. TEM analysis showed that ball-milling generated an amorphous layer on the clathrate surface, which is crucial for the electrochemical reaction with Li. The ball-milling process increased the capacity of the clathrate from 85 mAh/g to 472 mAh/g. The XPS and Raman spectroscopy results suggested that a new oxide layer was introduced by the acid/base treatment, which inhibited the lithiation due to a high charge transfer impedance and led to a decreased capacity of 126 mAh/g. Further ball-milling can expose the clathrate surface again and decrease the particle size, resulting in capacities of 176 mAh/g and 403 mAh/g in the samples ball-milled for 40 and 120 min, respectively. According to the XRD analysis, all the lithiation/delithiation processes are proposed to occur in single phase reactions as there is no discernible structure change. The EIS and dQ analysis support a surface-dominated Faradaic process for lithiation, which is different from the Warburg diffusion mechanism in conventional silicon anodes. This work elucidates some of the important structural and compositional parameters that should be considered when designing silicon clathrate electrodes for energy storage applications.

ASSOCIATED CONTENT

Supporting Information

The Supporting Information is available free of charge on the ACS Publications website at DOI: 10.1021/acsami.7b12810.

Experimental methods and characterization details; zoomed in view of the powder XRD pattern for AM-1 and HP; XRD patterns for clathrates at high angles and after first charge and 100 cycles; cell parameters for clathrate samples; microprobe analysis results; deconvolution of Si 2*p* XPS signal; capacity vs cycle number under galvanostatic cycling; differential capacity plots of AM-3 without carbon black and Al_2O_3 composite electrode; voltage profile of galvanostatic testing procedures for EIS measurements; equivalent circuits and fitted Nyquist plots; fitted circuit parameters (PDF)

Crystallographic information file (CIF) of AM-1 obtained from single crystal XRD (CIF)

AUTHOR INFORMATION

Corresponding Author

*Phone: (480) 727-8614; e-mail: candace.chan@asu.edu.

ORCID

Svilen Bobev: 0000-0002-0780-4787

Candace K. Chan: 0000-0003-4329-4865

Author Contributions

The manuscript was written through contributions of all authors. R.Z. prepared the electrodes, performed the electrochemical measurements, XRD, SEM, and XPS analysis. S.B. prepared the samples using arc-melting and L.K. prepared the samples using hot-pressing. T.Y. assisted with TEM, H.J. with XPS, and J.M.W. with Raman spectroscopy. C.K.C. conceived the project and performed the electrochemical analysis. All authors have given approval to the final version of the manuscript.

Notes

The authors declare no competing financial interest.

ACKNOWLEDGMENTS

This work was supported by funding from NSF DMR-1206795. We thank Y. Li for helpful discussions. We greatly acknowledge the use of facilities within the LeRoy Eyring Center for Solid State Science at Arizona State University. Support for the synthesis of Zintl clathrates by L.K. was provided by Energy Frontier Research in Extreme Environments (EFree) Center, an Energy Frontier Research Center funded by the U.S. Department of Energy, Office of Science under award No. DE-SC0001057.

REFERENCES

(1) Kasper, J. S.; Hagenmuller, P.; Pouchard, M.; Cros, C. Clathrate Structure of Silicon Na_8Si_{46} and Na_xSi_{136} ($x < 11$). *Science* **1965**, *150*, 1713−1714.

(2) Kawaji, H.; Horie, H.; Yamanaka, S.; Ishikawa, M. Superconductivity in the Silicon Clathrate Compound $(Na, Ba)_xSi_{46}$. *Phys. Rev. Lett.* **1995**, *74* (8), 1427−1429.

(3) Reny, E.; San-Miguel, A.; Guyot, Y.; Masenelli, B.; Mélinon, P.; Saviot, L.; Yamanaka, S.; Champagnon, B.; Cros, C.; Pouchard, M.; Borowski, M.; Dianoux, A. J. Vibrational Modes in Silicon Clathrate Compounds: A Key to Understanding Superconductivity. *Phys. Rev. B: Condens. Matter Mater. Phys.* **2002**, *66* (1), 014532.

(4) Connétable, D.; Timoshevskii, V.; Masenelli, B.; Beille, J.; Marcus, J.; Barbara, B.; Saitta, A. M.; Rignanese, G.-M.; Mélinon, P.; Yamanaka, S.; Blasé, X. Superconductivity in Doped sp^3 Semiconductors: The Case of the Clathrates. *Phys. Rev. Lett.* **2003**, *91* (24), 247001.

(5) Kume, K.; Kawaji, H.; Yamanaka, S.; Ishikawa, M. NMR Study in the Superconducting Silicon Clathrate Compound $Na_xBa_ySi_{46}$. *Phys. Rev. B* **1996**, *54* (18), 242−246.

(6) Herrmann, R. F. W.; Tanigaki, K.; Kuroshima, S.; Suematsu, H. Superconductivity in Silicon Based Barium-Inclusion Clathrates. *Chem. Phys. Lett.* **1998**, *283*, 29−32.

(7) Yamanaka, S.; Enishi, E.; Fukuoka, H.; Yasukawa, M. High-Pressure Synthesis of a New Silicon Clathrate Superconductor, Ba_8Si_{46}. *Inorg. Chem.* **2000**, *39* (1), 56−58.

(8) Kume, T.; Fukuoka, H.; Koda, T.; Sasaki, S.; Shimizu, H.; Yamanaka, S. High-Pressure Raman Study of Ba Doped Silicon Clathrate. *Phys. Rev. Lett.* **2003**, *90* (15), 155503.

(9) Fukuoka, H.; Kiyoto, J.; Yamanaka, S. Superconductivity of Metal Deficient Silicon Clathrate Compounds, $Ba_{8-x}Si_{46}$ ($0 < X < 1.4$). *Inorg. Chem.* **2003**, *42* (9), 2933−2937.
(10) Toulemonde, P.; Adessi, C.; Blase, X.; San Miguel, A.; Tholence, J. L. Superconductivity in the $(Ba_{1-x}Sr_x)_8Si_{46}$ Clathrates ($x \leq 0.75$): Experimental and Ab Initio Investigation. *Phys. Rev. B: Condens. Matter Mater. Phys.* **2005**, *71* (9), 094504.
(11) Blake, N. P.; Mollnitz, L.; Kresse, G.; Metiu, H. Why Clathrates Are Good Thermoelectrics: A Theoretical Study of $Sr_8Ga_{16}Ge_{30}$. *J. Chem. Phys.* **1999**, *111* (7), 3133−3144.
(12) Nolas, G. S.; Slack, G. A.; Schujman, S. B. Chapter 6 Semiconductor Clathrates: A Phonon Glass Electron Crystal Material with Potential for Thermoelectric Applications. *Semicond. Semimetals* **2001**, *69*, 255−300.
(13) Tsujii, N.; Roudebush, J. H.; Zevalkink, A.; Cox-Uvarov, C. A.; Jeffery Snyder, G.; Kauzlarich, S. M. Phase Stability and Chemical Composition Dependence of the Thermoelectric Properties of the Type-I Clathrate $Ba_8Al_xSi_{46-x}$ ($8 \leq x \leq 15$). *J. Solid State Chem.* **2011**, *184* (5), 1293−1303.
(14) Condron, C. L.; Martin, J.; Nolas, G. S.; Piccoli, P. M. B.; Schultz, A. J.; Kauzlarich, S. M. Structure and Thermoelectric Characterization of $Ba_8Al_{14}Si_{31}$. *Inorg. Chem.* **2006**, *45* (23), 9381−9386.
(15) Condron, C. L.; Kauzlarich, S. M.; Nolas, G. S. Structure and Thermoelectric Characterization of $A_xBa_{8-x}Al_{14}Si_{31}$ (A = Sr, Eu) Single Crystals. *Inorg. Chem.* **2007**, *46* (7), 2556−2562.
(16) Condron, C. L.; Kauzlarich, S. M.; Ikeda, T.; Jeffery Snyder, G.; Haarmann, F.; Jeglic, P. Synthesis, Structure, and High-Temperature Thermoelectric Properties of Boron-Doped $Ba_8Al_{14}Si_{31}$ Clathrate I Phases. *Inorg. Chem.* **2008**, *47* (18), 8204−8212.
(17) Christensen, M.; Johnsen, S.; Iversen, B. B. Thermoelectric Clathrates of Type I. *Dalton Trans.* **2010**, *39* (4), 978−992.
(18) Cros, C.; Pouchard, M.; Hagenmuller, P. Sur Une Nouvelle Famille de Clathrates Mineraux Isotypes Des Hydrates de Gaz et de Liquides. Interpretation Des Resultats Obtenus. *J. Solid State Chem.* **1970**, *2* (4), 570−581.
(19) Mott, N. F. Properties of Compounds of Type Na_xSi_{46} and Na_xSi_{136}. *J. Solid State Chem.* **1973**, *6* (3), 348−351.
(20) Baranowski, L. L.; Krishna, L.; Martinez, A. D.; Raharjo, T.; Stevanović, V.; Tamboli, A. C.; Toberer, E. S. Synthesis and Optical Band Gaps of Alloyed Si−Ge Type II Clathrates. *J. Mater. Chem. C* **2014**, *2* (17), 3231−3237.
(21) Martinez, A. D.; Krishna, L.; Baranowski, L. L.; Lusk, M. T.; Toberer, E. S.; Tamboli, A. C. Synthesis of Group IV Clathrates for Photovoltaics. *IEEE J. Photovoltaics* **2013**, *3* (4), 1305−1310.
(22) Neiner, D.; Okamoto, N. L.; Condron, C. L.; Ramasse, Q. M.; Yu, P.; Browning, N. D.; Kauzlarich, S. M. Hydrogen Encapsulation in a Silicon Clathrate Type I Structure: $Na_{5.5}(H_2)_{2.15}Si_{46}$: Synthesis and Characterization. *J. Am. Chem. Soc.* **2007**, *129* (45), 13857−13862.
(23) Neiner, D.; Okamoto, N. L.; Yu, P.; Leonard, S.; Condron, C. L.; Toney, M. F.; Ramasse, Q. M.; Browning, N. D.; Kauzlarich, S. M. Synthesis and Characterization of $K_{8-x}(H_2)_ySi_{46}$. *Inorg. Chem.* **2010**, *49* (3), 815−822.
(24) San-Miguel, A.; Kéghélian, P.; Blase, X.; Mélinon, P.; Perez, A.; Itié, J.; Polian, A.; Reny, E.; Cros, C.; Pouchard, M. High Pressure Behavior of Silicon Clathrates: A New Class of Low Compressibility Materials. *Phys. Rev. Lett.* **1999**, *83* (25), 5290−5293.
(25) Eisenmann, B.; Schäfer, H.; Zagler, R. Die Verbindungen $A_8^{II}B_{16}^{III}B_{30}^{IV}$ (A^{II} = Sr,Ba; B^{III} = Al,Ga; B^{IV} = Si,Ge,Sn) Und Ihre Käfigstrukturen. *J. Less-Common Met.* **1986**, *118*, 43−55.
(26) Cordier, G.; Woll, P. Neue Ternäre Intermetallische Verbindungen Mit Clathratstruktur: $Ba_8(T,Si)_6Si_{40}$ Und $Ba_6(T,Ge)_6Ge_{40}$ Mit T ≡ Ni, Pd, Pt, Cu, Ag, Au. *J. Less-Common Met.* **1991**, *169* (2), 291−302.
(27) Yan, X.; Giester, G.; Bauer, E.; Rogl, P.; Paschen, S. Ba-Cu-Si Clathrates: Phase Equilibria and Crystal Chemistry. *J. Electron. Mater.* **2010**, *39* (9), 1634−1639.
(28) Schäfer, H.; Eisenmann, B.; Muller, W. Zintl Phases: Transitions between Metallic and Ionic Bonding. *Angew. Chem., Int. Ed. Engl.* **1973**, *12* (9), 694−712.
(29) Schäfer, H. On the Problem of Polar Intermetallic Compounds: The Stimulation of E. Zintl's Work for the Modern Chemistry of Intermetallics. *Annu. Rev. Mater. Sci.* **1985**, *15*, 1−41.
(30) Mudryk, Y.; Rogl, P.; Paul, C.; Berger, S.; Bauer, E.; Hilscher, G.; Godart, C.; Noel, H. Thermoelectricity of Clathrate I Si and Ge Phases. *J. Phys.: Condens. Matter* **2002**, *14*, 7991−8004.
(31) Okamoto, N. L.; Oh, M. W.; Nishii, T.; Tanaka, K.; Inui, H. Crystal Structure and Thermoelectric Properties of the Type-I Clathrate Compound Ba_8Ge_{43} with an Ordered Arrangement of Ge Vacancies. *J. Appl. Phys.* **2006**, *99* (3), 033513.
(32) Kaltzoglou, A.; Hoffmann, S. D.; Fässler, T. F. Order-Disorder Phase Transition in Type-I Clathrate $Cs_8Sn_{44}\square_2$. *Eur. J. Inorg. Chem.* **2007**, *2007* (26), 4162−4167.
(33) Langer, T.; Dupke, S.; Trill, H.; Passerini, S.; Eckert, H.; Pöttgen, R.; Winter, M. Electrochemical Lithiation of Silicon Clathrate-II. *J. Electrochem. Soc.* **2012**, *159159* (885), 1318−1322.
(34) Yang, J.; Tse, J. S. Silicon Clathrates as Anode Materials for Lithium Ion Batteries? *J. Mater. Chem. A* **2013**, *1* (26), 7782−7789.
(35) Wagner, N. A.; Raghavan, R.; Zhao, R.; Wei, Q.; Peng, X.; Chan, C. K. Electrochemical Cycling of Sodium-Filled Silicon Clathrate. *ChemElectroChem* **2014**, *1* (2), 347−353.
(36) Li, Y.; Raghavan, R.; Wagner, N. A.; Davidowski, S. K.; Baggetto, L.; Zhao, R.; Cheng, Q.; Yarger, J. L.; Veith, G. M.; Ellis-Terrell, C.; Miller, M. A.; Chan, K. S.; Chan, C. K. Type I Clathrates as Novel Silicon Anodes: An Electrochemical and Structural Investigation. *Adv. Sci.* **2015**, *2* (6), 1500057.
(37) Peng, X.; Wei, Q.; Li, Y.; Chan, C. K. First-Principles Study of Lithiation of Type I Ba-Doped Silicon Clathrates. *J. Phys. Chem. C* **2015**, *119* (51), 28247−28257.
(38) Chan, K. S.; Miller, M. A.; Liang, W.; Ellis-Terrell, C.; Chan, C. K. First Principles and Experimental Studies of Empty Si_{46} as Anode Materials for Li-Ion Batteries. *J. Mater. Res.* **2016**, *31* (23), 3657−3665.
(39) Warrier, P.; Koh, C. A. Silicon Clathrates for Lithium Ion Batteries: A Perspective. *Appl. Phys. Rev.* **2016**, *3* (4), 040805.
(40) Liu, B.; Jia, X.; Sun, H.; Sun, B.; Zhang, Y.; Liu, H.; Kong, L.; Huo, D.; Ma, H. HPHT Synthesis, Structure and Electrical Properties of Type-I Clathrates $Ba_8Al_xSi_{46-x}$. *J. Solid State Chem.* **2016**, *233*, 363−367.
(41) Aydemir, U.; Candolfi, C.; Ormeci, A.; Borrmann, H.; Burkhardt, U.; Oztan, Y.; Oeschler, N.; Baitinger, M.; Steglich, F.; Grin, Y. Synthesis, Crystal Structure, and Physical Properties of the Type-I Clathrate $Ba_{8-\delta}Ni_x\square_ySi_{46-x-y}$. *Inorg. Chem.* **2012**, *51*, 4730−4741.
(42) Anno, H.; Shirataki, R. Effect of Heat Treatment in Air on the Surface of a Sintered $Ba_8Al_{16}Si_{30}$-Based Clathrate. *J. Electron. Mater.* **2014**, *43* (6), 1847−1856.
(43) Troppenz, M.; Rigamonti, S.; Draxl, C. Predicting Ground-State Configurations and Electronic Properties of the Thermoelectric Clathrates $Ba_8Al_XSi_{46-X}$ and $Sr_8Al_XSi_{46-X}$. *Chem. Mater.* **2017**, *29* (9), 2414−2424.
(44) Nagatomo, Y.; Mugita, N.; Nakakohara, Y.; Saisho, M.; Tajiri, M.; Teranishi, R.; Munetoh, S. Thermoelectric Properties of Single Crystalline $Ba_8Al_xSi_{46-x}$ Clathrate by Using Flux Czochralski Method. *J. Phys. Conf. Ser.* **2012**, *379* (1), 12008.
(45) Barr, T. L. An XPS Study of Si as It Occurs in Adsorbents, Catalysts, and Thin Films. *Appl. Surf. Sci.* **1983**, *15* (1−4), 1−35.
(46) He, J.; Klug, D. D.; Uehara, K.; Preston, K. F.; Ratcliffe, C. I.; Tse, J. S. NMR and X-Ray Spectroscopy of Sodium−Silicon Clathrates. *J. Phys. Chem. B* **2001**, *105* (17), 3475−3485.
(47) Kume, T.; Koda, T.; Sasaki, S.; Shimizu, H.; Tse, J. S. High-Pressure Raman Study of the Potassium-Doped Silicon Clathrate K_8Si_{46}. Phys. *Phys. Rev. B: Condens. Matter Mater. Phys.* **2004**, *70* (5), 1−4.
(48) Shimizu, H.; Kume, T.; Kuroda, T.; Sasaki, S.; Fukuoka, H.; Yamanaka, S. High-Pressure Raman Study of the Ba-Doped Silicon

DOI: 10.1021/acsami.7b12810
ACS Appl. Mater. Interfaces 2017, 9, 41246−41257

Clathrate $Ba_{24}Si_{100}$ up to 27 GPa. Phys. *Phys. Rev. B: Condens. Matter Mater. Phys.* **2005**, *71* (9), 1−5.
(49) Condron, C. L.; Porter, R.; Guo, T.; Kauzlarich, S. M. Crystal Structures, Raman Spectroscopy, and Magnetic Properties of $Ba_{7.5}Al_{13}Si_{29}$ and $Eu_{0.27}Ba_{7.22}Al_{13}Si_{29}$. *Inorg. Chem.* **2005**, *44* (25), 9185−9191.
(50) Shimizu, H.; Iitaka, T.; Fukushima, T.; Kume, T.; Sasaki, S.; Sata, N.; Ohishi, Y.; Fukuoka, H.; Yamanaka, S. Raman and X-Ray Diffraction Studies of Ba Doped Germanium Clathrate Ba_8Ge_{43} at High Pressures. *J. Appl. Phys.* **2007**, *101* (6), 063549.
(51) Nenghabi, E. N.; Myles, C. W. First Principles Calculations of the Structural, Electronic and Vibrational Properties of the Clathrates $Ba_8Al_{16}Ge_{30}$ and $Ba_8Al_{16}Si_{30}$. *J. Phys.: Condens. Matter* **2008**, *20* (41), 415214.
(52) Schroder, K. W.; Celio, H.; Webb, L. J.; Stevenson, K. J. Examining Solid Electrolyte Interphase Formation on Crystalline Silicon Electrodes: Influence of Electrochemical Preparation and Ambient Exposure Conditions. *J. Phys. Chem. C* **2012**, *116* (37), 19737−19747.
(53) Simon, P.; Gogotsi, Y. Materials for Electrochemical Capacitors. *Nat. Mater.* **2008**, *7* (11), 845−854.
(54) Kim, S. O.; Manthiram, A. Low-Cost Carbon-Coated Si-Cu_3Si-Al_2O_3 Nanocomposite Anodes for High-Performance Lithium-Ion Batteries. *J. Power Sources* **2016**, *332*, 222−229.
(55) Obrovac, M. N.; Christensen, L. Structural Changes in Silicon Anodes during Lithium Insertion/Extraction. *Electrochem. Solid-State Lett.* **2004**, *7* (5), A93−A96.
(56) Li, J.; Dahn, J. R. An In Situ X-Ray Diffraction Study of the Reaction of Li with Crystalline Si. *J. Electrochem. Soc.* **2007**, *154* (3), A156−A161.
(57) Hatchard, T. D.; Dahn, J. R. In Situ XRD and Electrochemical Study of the Reaction of Lithium with Amorphous Silicon. *J. Electrochem. Soc.* **2004**, *151* (6), A838−A842.
(58) Kim, T.; Park, S.; Oh, S. M. Solid-State NMR and Electrochemical Dilatometry Study on Li^+ Uptake/Extraction Mechanism in SiO Electrode. *J. Electrochem. Soc.* **2007**, *154* (12), A1112−A11117.
(59) Ruffo, R.; Hong, S. S.; Chan, C. K.; Huggins, R. A.; Cui, Y. Impedance Analysis of Silicon Nanowire Lithium Ion Battery Anodes. *J. Phys. Chem. C* **2009**, *113*, 11390−11398.
(60) Song, J. Y.; Lee, H. H.; Wang, Y. Y.; Wan, C. C. Two- and Three-Electrode Impedance Spectroscopy of Lithium-Ion Batteries. *J. Power Sources* **2002**, *111*, 255−267.
(61) La Mantia, F.; Vetter, J.; Novák, P. Impedance spectroscopy on porous materials: a general model and application to graphite electrodes of lithium-ion batteries. *Electrochim. Acta* **2008**, *53*, 4109−4121.
(62) Chang, Y. C.; Sohn, H. J. Electrochemical Impedance Analysis for Lithium Ion Intercalation into Graphitized Carbons. *J. Electrochem. Soc.* **2000**, *147* (1), 50−58.
(63) Holzapfel, M.; Martinent, A.; Alloin, F.; Le Gorrec, B.; Yazami, R.; Montella, C. First Lithiation and Charge/Discharge Cycles of Graphite Materials, Investigated by Electrochemical Impedance Spectroscopy. *J. Electroanal. Chem.* **2003**, *546*, 41−50.
(64) Fan, X.-Y.; Zhuang, Q.; Wei, G.; Huang, L.; Dong, Q.-F.; Sun, S.-G. One-Step Electrodeposition Synthesis and Electrochemical Properties of Cu_6Sn_5 Alloy Anodes for Lithium-Ion Batteries. *J. Appl. Electrochem.* **2009**, *39*, 1323−1330.
(65) Sugimoto, W.; Iwata, H.; Yokoshima, K.; Murakami, Y.; Takasu, Y. Proton and Electron Conductivity in Hydrous Ruthenium Oxides Evaluated by Electrochemical Impedance Spectroscopy: The Origin of Large Capacitance. *J. Phys. Chem. B* **2005**, *109*, 7330−7338.
(66) Farsi, H.; Gobal, F.; Raissi, H.; Moghiminia, S. On the Pseudocapacitive Behavior of Nanostructured Molybdenum Oxide. *J. Solid State Electrochem.* **2010**, *14*, 643−650.
(67) Nilson, R. H.; Brumbach, M. T.; Bunker, B. C. Modeling the Electrochemical Impedance Spectra of Electroactive Pseudocapacitive Materials. *J. Electrochem. Soc.* **2011**, *158* (6), A678−A688.
(68) Paloukis, F.; Elmasides, C.; Farmakis, F.; Selinis, P.; Neophytides, S. G.; Georgoulas, N. Electrochemical Impedance Spectroscopy Study in Micro-Grain Structured Amorphous Silicon Anodes for Lithium-Ion Batteries. *J. Power Sources* **2016**, *331*, 285−292.
(69) Campbell, B.; Ionescu, R.; Tolchin, M.; Ahmed, K.; Favors, Z.; Bozhilov, K. N.; Ozkan, C. S.; Ozkan, M. Carbon-Coated, Diatomite-Derived Nanosilicon as a High Rate Capable Li-Ion Battery Anode. *Sci. Rep.* **2016**, *6*, 33050.
(70) Liang, Y.; Böhme, B.; Ormeci, A.; Borrmann, H.; Pecher, O.; Haarmann, F.; Schnelle, W.; Baitinger, M.; Grin, Y. A Clathrate-I Phase with Li-Ge Framework. *Chem. - Eur. J.* **2012**, *18* (32), 9818−9822.
(71) Böhme, B.; Wei, K.; Bobnar, M.; Prots, Y.; Burkhardt, U.; Baitinger, M.; Nolas, G. S.; Grin, Y. A Type-II Clathrate with a Li-Ge Framework. *Z. Kristallogr. - Cryst. Mater.* **2017**, *232* (7−9), 543−556.

DOI: 10.1021/acsami.7b12810
ACS Appl. Mater. Interfaces 2017, 9, 41246−41257